



Pyranoid-O-dominated graphene-like nanocarbon for two-electron oxygen reduction reaction

Chang Zhang^{a,1}, Wei Liu^{a,1}, Min Song^a, Jingjing Zhang^a, Feng He^a, Jiao Wang^b, Mo Xiong^c, Jian Zhang^{a,*}, Deli Wang^{a,*}

^a Key Laboratory of Material Chemistry for Energy Conversion and Storage, Ministry of Education, Hubei Key Laboratory of Material Chemistry and Service Failure, School of Chemistry and Chemical Engineering, Huazhong University of Science and Technology, Wuhan 430074, People's Republic of China

^b State Key Laboratory of Coal Combustion, Huazhong University of Science and Technology, Wuhan 430074, People's Republic of China

^c MOE Key Laboratory for Non-Equilibrium Synthesis and Modulation of Condensed Matter, School of Physics, Xi'an Jiaotong University, Xi'an 710049 Shaanxi, People's Republic of China

ARTICLE INFO

Keywords:

Oxygen reduction reaction
Electrocatalyst
Carbonaceous materials
Two-electron selectivity
Hydrogen peroxide electrosynthesis

ABSTRACT

Exploring the high-efficient two-electron oxygen reduction reaction ($2e^-$ ORR) catalysts is greatly significant for promoting hydrogen peroxide (H_2O_2) electroproduction. Herein, we have constructed a pyranoid-O-dominated graphene-like nanocarbon (GLC) material with high surface area, hierarchical porous structure, and abundant edge defects, through the high-temperature alkali activation of cellulose-based precursor. Benefiting from its integrated merits, the GLC electrocatalyst exhibits excellent $2e^-$ ORR performance with high H_2O_2 productivity and ultrafast wastewater degradation ability. Interestingly, whether changing the carbonaceous precursor or alkali activator, all the as-prepared pyranoid-O-dominated GLC-based materials display high $2e^-$ selectivity for the ORR. Based on further analogical experiments and theoretical analysis, the results reveal that the nature of $2e^-$ selectivity on carbon-based materials is highly associated with the pyranoid-O dopants, rather than the surface oxygen-containing functional groups declared by the previous reports. These findings may bring new insight into the $2e^-$ ORR selectivity of carbon-based electrocatalysts for H_2O_2 production.

1. Introduction

Hydrogen peroxide (H_2O_2) has been extensively utilizing in chemical industries, medicine, and environmental remediation fields as a green oxidant [1–4]. As reported, the yearly global consumption of H_2O_2 is about 4 million tons to date and expects to reach 6.0 million tons in the next few years [5]. Until now, 95% of H_2O_2 is generated through an anthraquinone oxidation process, which not only requires a lot of energy input, but also accompanies vast waste generation [3–7]. In addition, the high concentrated H_2O_2 product (~ 70 wt%) may bring safety hazards during the storage and transportation process owing to its instability [7]. Thus, the development of energy-saving, pollution-free, and on-site property methods for H_2O_2 production has aroused more and more interest in people. In this regard, the electroproduction process via a two-electron oxygen reduction reaction ($2e^-$ ORR) is considered to be one of the most promising approaches, because it only needs electricity, O_2 (from the air), and water resources that features energy efficiency,

low cost, environmental friendliness, and decentralized production [4–11]. However, this process greatly suffers from the sluggish kinetics and low selectivity ($2e^-$) of ORR in the cathode [6–16]. Thus, the exploitation of highly efficient $2e^-$ ORR catalysts is greatly significant for H_2O_2 electrosynthesis.

Carbon-based catalysts have attracted extra attention for H_2O_2 electrosynthesis because they have multi advantages such as cost-effectiveness, rich resources, and surface structure tunability [17–20]. Among all the carbon-based candidates, graphene-based materials exhibited great potential for ORR owing to their high conductivity, specific surface area, mass transfer rate, and durability [21–25]. However, the current graphene manufacturing methods such as chemical vapor deposition [26], redox process [27], liquid phase stripping [28], etc., are comparatively complicated and hard-conditioned, which are not in favor of large-scale application and sustainable development. Thus, finding a facile and cost-effective way for the construction of graphene-based material with a functional application is highly

* Corresponding authors.

E-mail addresses: zhangjian7@hust.edu.cn (J. Zhang), wangdl81125@hust.edu.cn (D. Wang).

¹ Chang Zhang and Wei Liu contributed equally to this work

expected. Normally, the oxygen functionalized carbon materials such as oxidized carbon nanotubes, graphene nanobelt, carbon nanofiber, etc., present the excellent $2e^-$ ORR selectivity toward H_2O_2 synthesis [7]. However, owing to the complexity and diversity of oxygen species (e.g. $C=O$, $C-O-C$, $C-OOH$, $C-OH$, etc.) on the surface of carbon nanomaterials, the active sites is still controversial [29–32]. Therefore, ongoing research for the exploration of the real active species of carbon-based materials can further accelerate the design and development of catalysts for H_2O_2 electroproduction.

In light of this, we have constructed a pyranoid-O-dominated graphene-like nanocarbon (GLC) material for H_2O_2 electroproduction by using the high-temperature alkali activation process. This process was proved to be multi-functionalized including the graphene-like structures formation, pore creation, defect manufacture, and doping of oxygen atoms into the product. As a result, the prepared GLC material exhibits excellent electrocatalytic $2e^-$ ORR performance. In combination with theoretical calculation and experimental results, we prove that the outperformed $2e^-$ ORR performance of GLC is greatly associated with pyranoid-O dopants, which can efficiently alter the charge distribution of the carbon matrix to activate the neighboring carbon atoms, and meanwhile stabilize the intermediate $*OOH$ to boost the $2e^-$ ORR process. This finding will be greatly contributed to understanding the mechanism of oxygen functionalized carbon-based ORR electrocatalysts towards H_2O_2 synthesis.

2. Experimental section

2.1. Materials preparation

Firstly, the cellulose was pre-carbonized at 300 °C for 2 h in the Ar atmosphere. Then, it was mixed with KOH solution by the mass ratio of 1: 2 (KOH: pre-carbonized sample) under magnetic stirring. After utterly drying at 60 °C, the mixture was heated to 900 °C in Ar atmosphere with a rate of 5 °C/min and was activated at 900 °C for 2 h. Then, the sample was washed thoroughly for 12 h in 0.1 M HCl solution at 60 °C to remove the remaining KOH and the impurities. Finally, the GLC product was obtained by drying at 60 °C. For comparison, the bulk carbon (BC, without KOH activation) material was also prepared by direct pyrolysis of pre-carbonized cellulose at 900 °C in Ar atmosphere for 2 h.

To investigate the effect of activation temperature, the controlled samples activated at the temperatures of 700 °C, 800 °C, 900 °C, and 1000 °C (GLC-X, X = 700, 800, 900, and 1000) with a mass ratio of 1: 2 were prepared. The effect of the ratio of alkali and pre-carbonize cellulose was also studied, the controlled samples activated 900 °C with the alkali/carbon ratio of 1: 4, 1: 2, 1: 1, and 2: 1 (GLC-Y, Y=1/4, 1/2, 1, and 2) were prepared.

The reduced graphene-like nanocarbon (R-GLC) material was obtained by the treatment of GLC at 900 °C for 2 h in a mixed H_2 (5 vol%) /Ar atmosphere. The oxidized graphene-like nanocarbon (O-GLC) material was obtained by oxidizing GLC at 30% H_2O_2 solution for 12 h under magnetic stirring at room temperature.

The activated sawdust (AS) and activated bamboo (AB) samples were prepared under the same condition of GLC, except for using waste sawdust or bamboo scrap as the raw material. The GLC-NaOH and GLC- $KHCO_3$ samples were prepared under the same condition as GLC, except for using NaOH and $KHCO_3$ as the alkali agents, respectively.

3. Results and discussion

3.1. Materials preparation and characterization

The preparation procedure of GLC is exhibited in Fig. 1. First, cellulose was pre-carbonized to form the fluffy carbon. Then, it was mixed with KOH and activated at a high temperature. After acid washing and drying, the GLC product was finally obtained. During the KOH activation process, the intense reaction between KOH and carbon would produce large amounts of metallic K (Eq. (1)), which can embed into the carbon lattice, resulting in the reconstruction and self-organization of carbon atoms to form a graphene-like structure [33]. In addition, the violent reaction (Eq. (1)) and refactoring of K_2CO_3 (Eq. (2)) would generate a mass of gases (CO_2 , H_2 , CO , H_2O , etc.), which can be contributed to the formation of edge defects and nanopores in the carbon matrix [33]. Simultaneously, the oxygen-containing gases such as CO_2 and H_2O would be also reacted with the carbon, and be in-situ doping of oxygen element into the carbon skeleton, leading to an oxygen functionalized carbon product [31,32]. Thus, our as-obtained GLC material may possess graphene-like morphology, porous structure, abundant edge defects, as well as high content of oxygen dopant.



The scanning electron microscope (SEM) and transmission electron microscope (TEM) were first performed to investigate the morphology of GLC. As shown in Fig. 2a, b, GLC presents self-assembled nanosheets with interconnected macroporous structures. TEM images of Fig. 2c, d show that it also contains plenty of mesopores spanning from a few nanometers to tens of nanometers. The high angle annular dark field-TEM (HAADF-TEM) images of Fig. 2e can also prove the interconnected hierarchical porous and nanosheet-like structure of GLC. In contrast, the non-activated sample of bulk carbon (BC) sample has no obvious pore structure (Fig. S1), suggesting that the existence of KOH in the activation process can be greatly conducive to the formation of pores in the carbon material. From the high resolution-TEM (HR-TEM) image of Fig. 2f, GLC presents a well-defined nanosheets structure, which has only a few carbon layers, with a subtransparent property, as similar to the reported graphene morphology [34–36]. In addition, the irregular lattice along with plenty of micropores (white dots) are observed in Fig. 2f, indicating that GLC makes the feature of disorder and porous structure and abundant edge defects, which can also be attested by the selected area electron diffraction (SAED) pattern (inset of Fig. 2f) and X-ray diffraction (XRD) pattern (Fig. S2) of GLC.

For the exploration of the specific surface area and the pore structure

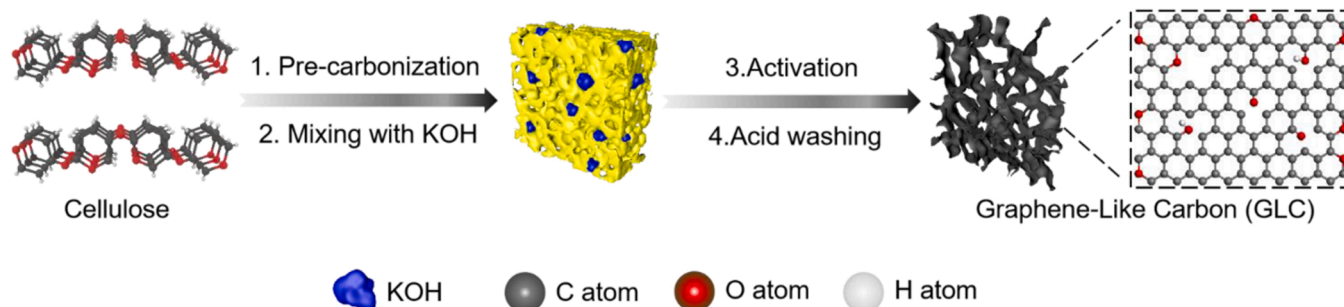


Fig. 1. Schematic illustration of the synthesis of GLC.

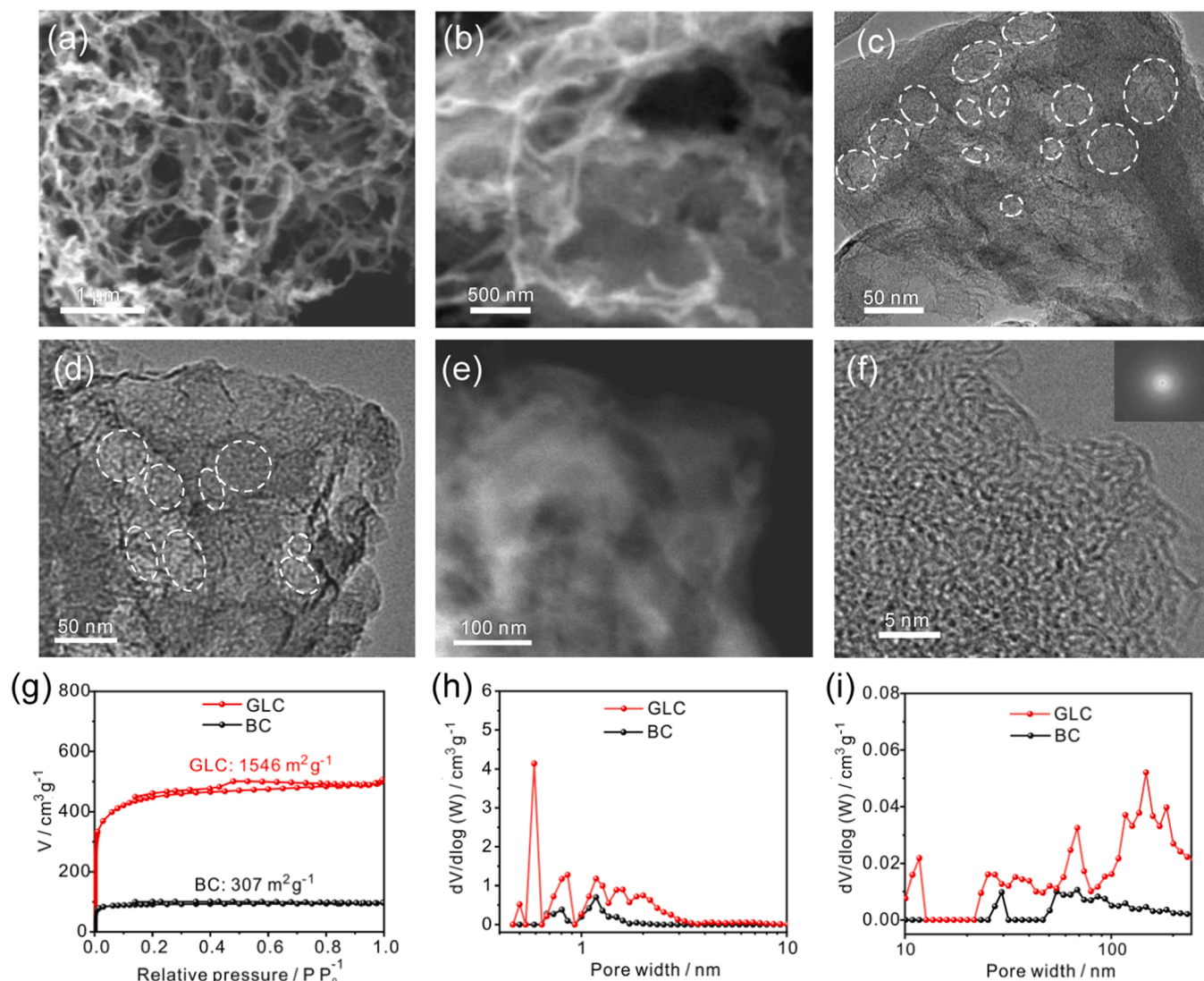


Fig. 2. (a,b) SEM and (c, d) TEM images of GLC. (e) HAADF-TEM and (f) HR-TEM image of GLC. The inset of Fig. 2f is the SAED pattern of GLC. (g) N_2 adsorption and desorption isotherms and (h, i) pore size distributions of BC and GLC.

of these samples, the N_2 adsorption and desorption isotherms measurements were performed, as displayed in Fig. 2g. Compared with the sample of BC, the GLC sample has a higher adsorption capacity, indicating the higher Brunauer–Emmett–Teller (BET) specific surface area ($1546 \text{ m}^2 \text{ g}^{-1}$). In addition, the GLC sample presents a composition of type I and IV isotherm curves with an obvious hysteresis loop, suggesting the hierarchically porous structure ranging from micro- to macropores [37,38], which is well confirmed by the pore diameter distribution diagrams of Fig. 2h, i. The high volume of micropores in carbon-based materials is conducive to providing a larger specific surface area and more active sites for the ORR, leading to a high H_2O_2 production rate [1]. In addition, the mesopores can enhance the mass transport of H_2O_2 into the electrolyte, avoiding subsequent reduction to H_2O [39]. For the BC sample, the BET surface area is only $307 \text{ m}^2 \text{ g}^{-1}$, and reveals a poor porosity. These results further prove the pore formation and delamination effect of KOH activation. In conclusion, our constructed GLC sample has graphene-like morphology, high surface area, hierarchical porous structure, plentiful edge defects, and abundant oxygen dopants, which can provide high conductivity, abundant active sites, and high mass activity for the electrocatalytic reactions.

Raman spectroscopy was used to probe the edge and defect information of these two samples. As exhibited in Fig. 3a, the disordered

carbon structure (D band) can be represented by the band at 1334 cm^{-1} , and the graphitic carbon (G band) is related to the band at 1576 cm^{-1} [40,41]. Notably, the characteristic of graphene-like property can be well defined by the 2D band at 2700 cm^{-1} [38]. The intensity ratio of the D band and G band (I_D/I_G) is usually utilized to assess the disorder level of carbon-based materials [38,42]. Strangely, the samples of GLC and BC present the same I_D/I_G value (1.02, Table S1). To precisely investigate the defective structure of these samples, the Raman spectra were further deconvoluted into five bands (Fig. 3b): polyenes at 1200 cm^{-1} (D_4 band), graphene layer edges at 1350 cm^{-1} (D_1 band), amorphous carbon at 1500 cm^{-1} (D_3 band), ideal graphitic lattice at 1580 cm^{-1} (G band), and surface graphene layers at 1620 cm^{-1} (D_2 band) [41]. In contrast to BC, GLC sample possesses higher area content of D_1 and D_2 band, while lower area content of D_4 , D_3 , and G band, suggesting that GLC has a higher proportion of graphene with edge defect layers, but a lower ratio of polyenes, amorphous carbon, and graphitic carbon lattice, further confirming the defect manufacture and delamination effect of KOH activation, which are in great agreement with the above-mentioned results.

The chemical features and surface states of produced samples are characterized by Fourier transform infrared spectra (FTIR) and X-ray photoelectron spectroscopy (XPS). As shown in Fig. 3c, the oxygen

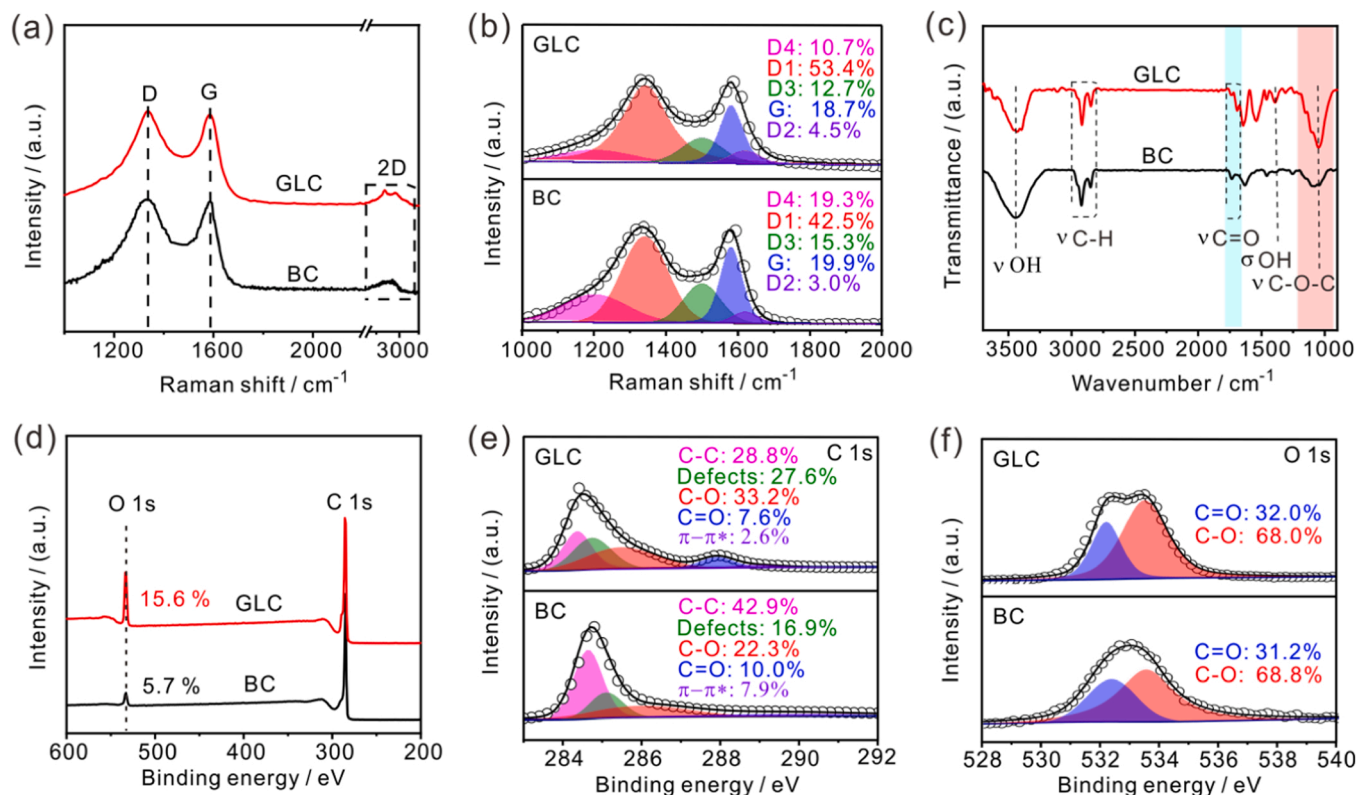


Fig. 3. (a) Raman and (b) deconvoluted Raman spectra of BC and GLC. (c) FTIR, and (d) survey XPS spectra of BC and GLC (the inset value is content of O 1s in these samples). Deconvoluted (e) C 1s, and (f) O 1s spectra of BC and GLC.

functional groups of both GLC and BC samples can be assigned to C–O–C at 1057 cm^{-1} , C–OH at 1380 cm^{-1} , and C=O, the shoulder peak at 1700 cm^{-1} [5], suggesting the existence of oxygen-containing species on

the surface of the samples. The survey XPS spectra (Fig. 3d and Table S2) expose that the atomic percent of O 1s of GLC (15.6%) is much higher than BC (5.7%), suggesting that KOH is conducive to the introduction of

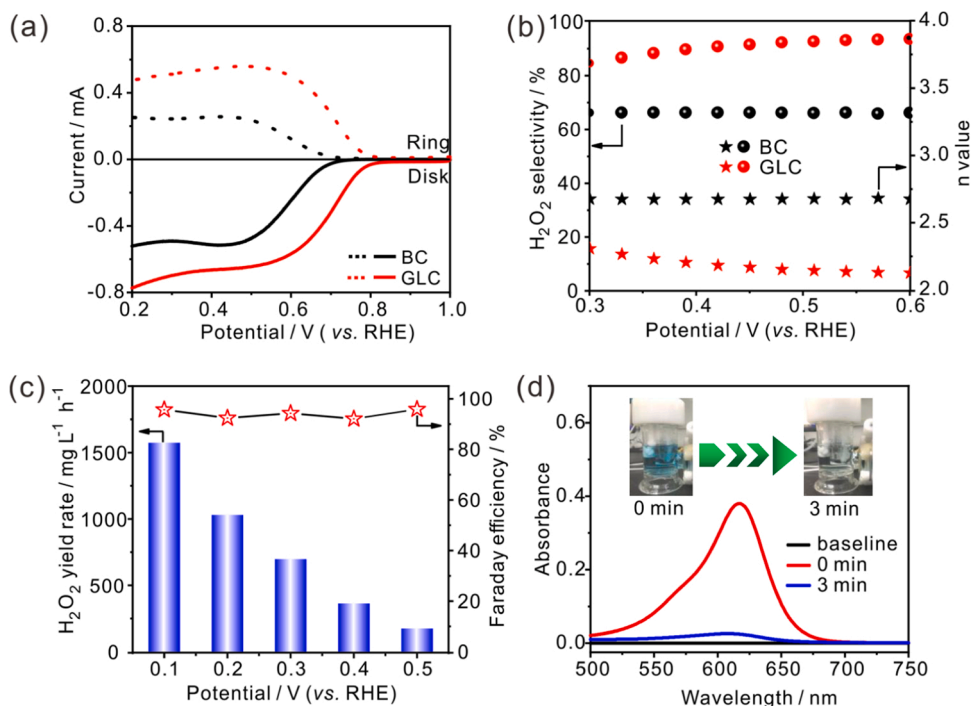


Fig. 4. (a) RRDE polarization curves (solid lines) and detective H₂O₂ currents at ring electrode (dot lines) of BC and GLC. (b) Calculated n value and H₂O₂ selectivity of BC and GLC. (c) The H₂O₂ yield rate and Faraday efficiency at different potentials. (d) The UV-vis spectra and photographs (inset pictures) of the malachite green solutions before and after 3 min of degradation.

oxygen in the carbon skeleton. Based on the well-established analysis [29,43], the XPS spectra were further deconvoluted, as exhibited in Fig. 3e, f. Quantifying the fitted C 1 s results (Table S3) suggest that the content of defects in GLC is higher than BC, which is in conformance with the Raman results. The O 1 s fitting results (Table S4) indicate that GLC and BC possess a similar ratio of C–O and C=O. However, considering the much higher total O 1 s content (Table S2), GLC owns a larger amount of doped oxygen content than that of BC. These characterization analyses manifest the key role of KOH in the activation process of the materials, which leads to the high content of oxygen dopants and defects in GLC.

3.2. Electrochemical performance

The electrocatalytic performance of the prepared samples (GLC and BC) was investigated by linear sweep voltammetry (LSV) on a three-electrode system at room temperature. First, by comparing the corresponding rotating ring-disk electrode (RRDE) polarization curves of a series of samples with different KOH and cellulose ratios, the best mass ratio of precursor (KOH: cellulose = 1: 2) was screened (Fig. S3). Thus, the following GLC samples were prepared under this ratio condition. Fig. 4a presents the RRDE measurement of GLC and BC catalysts. Compared to BC catalyst, GLC exhibits a higher onset potential (0.8 V), and higher currents on both disk and ring electrodes, meaning that GLC catalyst has a higher ORR activity and H₂O₂ production ability than BC. The calculated H₂O₂ selectivity and electron transfer number (*n*) value of GLC and BC catalysts in Fig. 4b describe that GLC owns a higher H₂O₂ selectivity compared with BC. Notably, the *n* value of the GLC catalyst almost approaches the benchmark value of 2. In addition, we can observe that, from detective H₂O₂ currents of the ring electrode, GLC presents a smaller Tafel slope than BC (Fig. S4), further demonstrating the fast H₂O₂ generation ability [31,44–46].

To investigate the connection between the 2e[−] ORR performance and character of the materials, a series of electrochemical measurements were performed. As displayed in Fig. S5, GLC has a lower equivalent series resistance (ESR) compared with BC, corresponding to a higher conductivity [47,48]. Furthermore, GLC also possesses a high electrochemical surface area (ECSA), as evidenced by the larger double-layer capacitance in Figs. S6 and S7. As reported, the graphene-like structure can deliver a high conductivity [47], the high surface area and the hierarchical porous structure can ensure a high active sites density and efficient oxygen diffusion [49], and the enriched edge defects and oxygen dopants can make the high electrocatalytic activity [50,51]. These multiple advantages would conspire to boost the 2e[−] ORR performance of GLC catalyst.

Apart from the outstanding ORR activity and H₂O₂ selectivity, stability is also very important for the catalyst. As shown in Fig. S8, there are negligible changes in both ring and disk current of GLC during the long-time testing, indicative of good electrochemical stability. The accelerated durability test (ADT) in Fig. S9 can also confirm this point. In addition, the morphology features of the sample (Fig. S10), which has been performed a long-term stability test, also shows the graphene-like morphology, hierarchical porous structure, and plentiful edge defects, indicating good physical stability of GLC. The 2e[−] ORR performance was also tested under acidic electrolytes, as shown in Fig. S11. Although the GLC sample also presents a high 2e[−] selectivity, the activity is poor. Summarizing the above characterization and experiment results, the KOH in the activation process plays the key role of stripping layers, forming pores and defects, and doping oxygen atoms in the product, so that the GLC sample features the graphene-like morphology, high surface area, hierarchical porous structure, plentiful edge defects, and abundant oxygen dopants, which contribute together to promote its electrocatalytic performance.

Considering the excellent 2e[−] ORR performance of GLC, the flow cell was assembled using GLC as the cathode catalyst to evaluate its actual H₂O₂ production performance. Fig. 4c reveals that the H₂O₂ yield rate of

GLC electrode can reach up to 1573.33 mg L^{−1} h^{−1}, with a Faraday efficiency of 95%, which is higher than most of the reported 2e[−] ORR catalysts (Table S5). In addition, the electro-Fenton-like system was constructed to simulate the industrial pollutants degradation process. Malachite green as an antibiotic or dyestuff is widely used for aquaculture or dye, whereas it is highly toxic to organisms and has been forbidden in many countries [52–55]. Thus, the degradation of malachite green is very significant. As shown in Fig. 4d, the device took only 3 min to completely degrade the malachite green solution (50 mg L^{−1} in 30 mL) at the potential of 0.1 V, suggesting the high degradation ability of GLC as the cathode catalyst in the electro-Fenton-like system. Overall, our constructed GLC catalyst exhibits a great application potential in H₂O₂ electroproduction and wastewater treatment.

Further, to probe the effect of KOH activation temperature, the controlled samples activated at different temperatures of 700 °C, 800 °C, 900 °C, and 1000 °C were prepared (labeled as GLC-X, X = 700, 800, 900, 1000). Raman spectra (Fig. 5a and Table S1) expose that the I_D/I_G value of the GLC-X samples increases with the increasing of activation temperature, suggesting that the defect degree is positive correlation with the temperature of the activation process. The deconvoluted Raman diagrams (Fig. S12) show that the area content of the D₁ and G band increases obviously whereas the area content of the D₃ band decreases with the increasing temperature, which suggests that the high temperature may convert the amorphous carbon into graphene with edge defects or/and graphite lattice. As a result, the samples activated at higher temperatures own a higher graphitization degree, which can be verified by the XRD results (Fig. S13). Moreover, the 2D graphene characteristic band is observed in all prepared materials, indicating that they all have a graphene-like structure. FTIR measurements (Fig. 5b) reveal that these samples own similar oxygen-containing species. From the XPS survey (Fig. 5c and Table S2), the atomic percent of O 1 s of these samples increases with the increasing of temperature, suggesting that high activation temperature is in favor of the introduction of oxygen elements into the carbon skeleton. These results indicate that the high temperature is conducive to increasing the defects, graphitization degree, and oxygen dopants of the material.

As shown in Fig. 5d, all the activated samples show a well-defined oxygen reduction current, suggesting the efficient electrocatalytic activities for ORR. Fig. 5e reveals that the on-set potential (*E*₀) of these samples increases as the activation temperature rises, whereas the peak current increases first and then decreases, indicating that high activation temperature is conducive to improve the ORR activity, but it is not necessarily good. The calculated H₂O₂ selectivity and *n* value (Fig. 5f) suggest that GLC-900 owns the highest 2e[−] selectivity. Balancing the electrocatalytic ORR activity and 2e[−] selectivity, the as-prepared GLC-900 sample at the activation temperature of 900 °C has the best 2e[−] ORR performance, which may be related to the appropriate defect and graphitization degree, the highest content of C–O species (Figs. S14 and S15), as well as the highest electroconductivity (Fig. S16). Therefore, the above GLC samples were constructed at the activation temperature of 900 °C.

Particularly and dramatically, our as-described strategy is not limited by the carbonaceous precursor or the alkali active agent, it has a certain universality. For example, when we use the waste sawdust or bamboo scrap as the precursor, they also show the same characteristic and electrochemical results, as compared with the series of GLC samples. As shown in Figs. S17 and S18, the similar Raman spectra and XRD patterns indicate that activated sawdust (AS) and activated bamboo (AB) possess a similar structure as GLC. FTIR results of Fig. S19 reveal that AS and AB have the same characteristic peaks (C–O–C, C=O, C–OH) as GLC, indicating that they own a similar surface state. The survey XPS spectra (Fig. S20) demonstrate that these samples also have abundant oxygen dopants. Thus, the obtained samples still have high ORR activity and 2e[−] selectivity for H₂O₂ synthesis (Fig. S21).

By changing the alkali agent of NaOH and KHCO₃, the prepared GLC-NaOH and GLC-KHCO₃ samples can also obtain a similar structure and

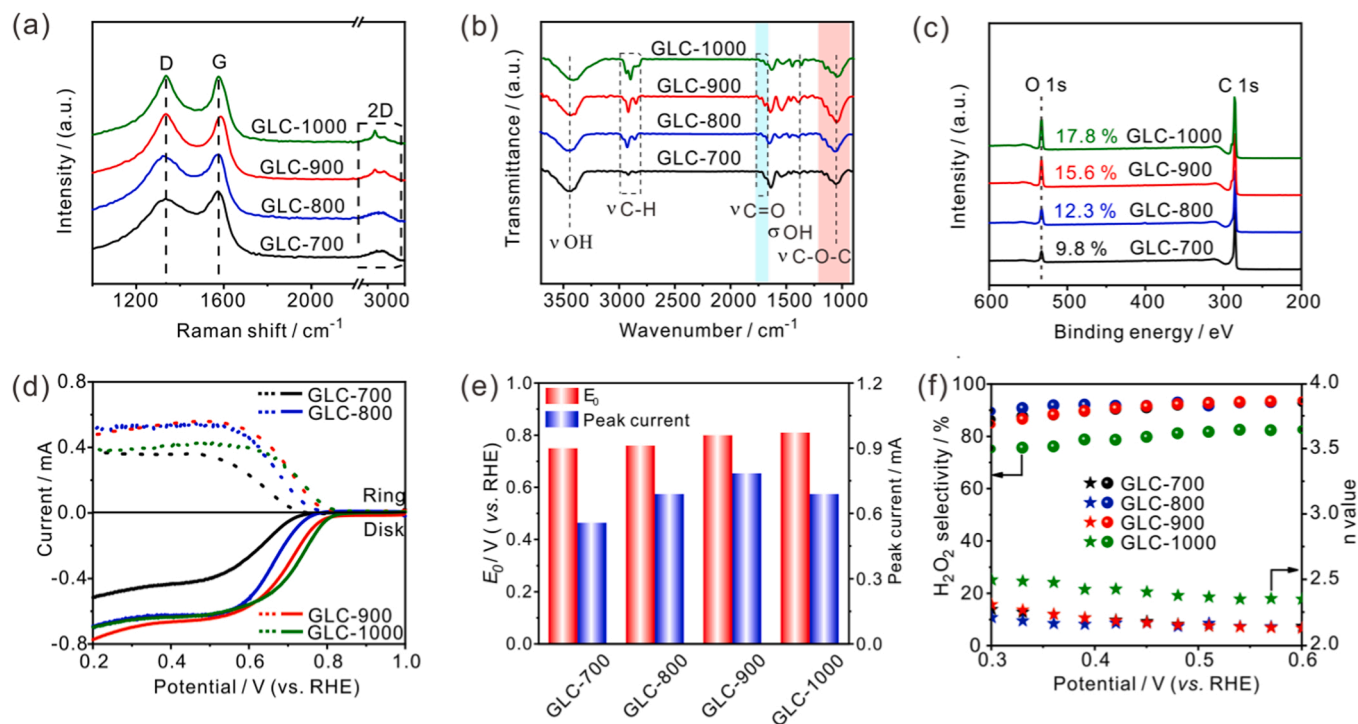


Fig. 5. (a) Raman, (b) FTIR, and (c) survey XPS spectra of GLC-X samples (the inset value is content of O 1 s in these samples). (d) RRDE polarization curves (soil lines) and detective H_2O_2 currents at ring electrode (dot lines) of GLC-X samples. (e) E_0 and peak current of GLC-X samples. (f) Calculated n value and H_2O_2 selectivity of GLC-X samples.

surface state as GLC, as evidenced by XRD, Raman, FTIR, and XPS results (Figs. S22-25). However, the lower O 1 s percentage of GLC-NaOH indicates that it has lower oxygen dopants, which may be related to the lower activity of metallic Na than K. As a result, GLC-NaOH shows a

worse $2e^-$ ORR performance (Fig. S26). Moreover, their $2e^-$ ORR performance can be well-tuned by adjusting the appropriate alkali/carbon ratio (Figs. S27-29).

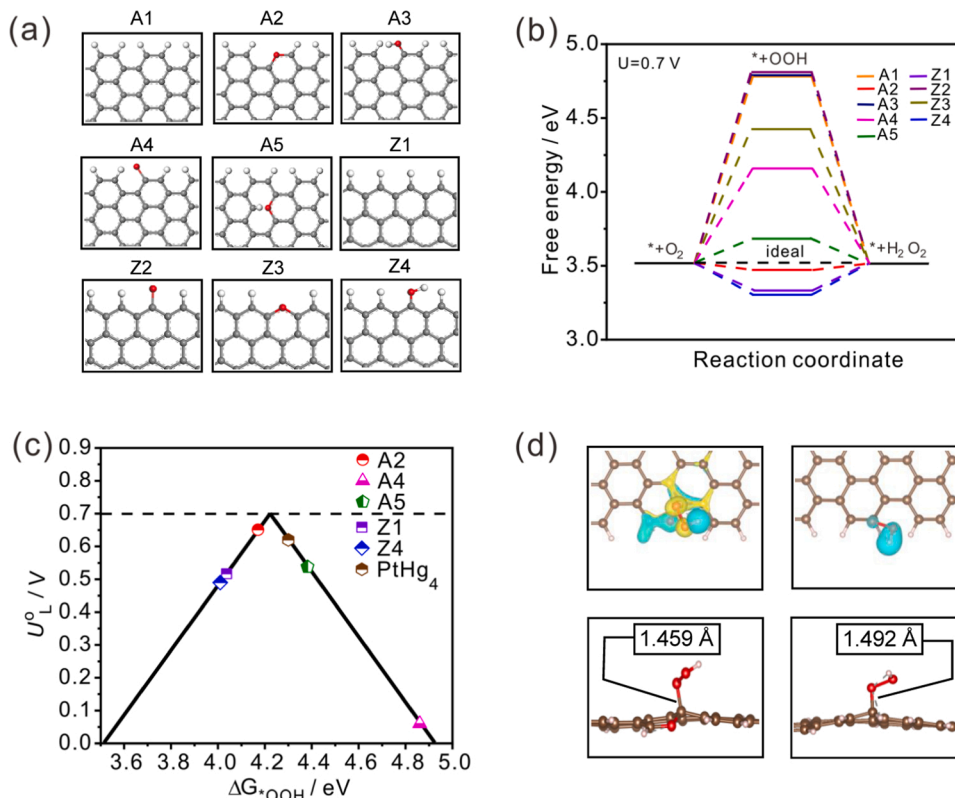


Fig. 6. (a) Configurations of different edge and oxygen doping types. (b) Standard free energy diagram of different systems for $2e^-$ ORR pathway at equilibrium potential of the reaction. (c) Volcano plot for $2e^-$ ORR displayed with U_0 as a function of ΔG^*_{OOH} . (d) The charge density difference of pyranoid-O doped armchair edges system and non-doped pure armchair edges system before and after interacting with $*OOH$, the isosurface is set to be 0.08 e per \AA , the yellow and cyan represent positive and negative charges, respectively. The brown hexagon exhibits the activity of $PtHg_4$ alloy adapted from reference [6].

3.3. Theoretical calculations and mechanism exploration

To disclose the nature of the excellent electrocatalytic performance of our prepared GLC samples, density functional theory (DFT) calculations were performed. Fig. 6a displays several models based on pure graphene sheet with or without C-OH, C=O, and C-O-C (also named as pyranoid-O) introduced on the zigzag edges or armchair edges. Based on the $2e^-$ ORR pathways, the standard free energy of the key intermediate of *OOH on each probable active site was obtained in Fig. 6b. Where the low free energy indicates strong adsorption to *OOH , in contrast, the high free energy means weak adsorption to *OOH . Based on the diagram, the pyranoid-O doped armchair system (A2) presents free energy of 3.47 eV, which approaches the ideal standard free energy of 3.52 eV, suggesting that pyranoid-O favors the ORR reaction towards the $2e^-$ route. According to the Sabatier principle, the activity of electrocatalyst for $2e^-$ ORR is determined by the adsorption/desorption properties of the *OOH [29]. Therefore, we use the *OOH adsorption free energy ($\Delta G_{^*OOH}$) as the descriptor to plot the activity volcano (Fig. 6c), where the limiting potential (U_L^0) is defined as the lowest potential when all elementary reaction steps can downhill [29]. Contrary to the oxygen-containing functional group (C-OH, C=O) introduced systems, the pyranoid-O doped armchair edges system locates nearly to the top, which is comparable to the noble metal-based alloy PtHg₄ [6], further suggesting that pyranoid-O can efficiently turn the ORR reaction to $2e^-$ pathway.

The electronic charge density difference of pyranoid-O doped armchair edges system (A2) and non-doped pure armchair edges system (A1) before and after the adsorption of intermediate *OOH was further investigated to understand how does the pyranoid-O improve the $2e^-$ ORR performance of the materials. As shown in Fig. 6d, the nearby electron of the active site is evenly distributed in A2, which means that the intermediate *OOH turns stable and binding affinitive with the site [56]. However, the A1 has a nearly undistributed electron, indicating the unstable intermediate and poor interaction between the site and *OOH [57]. As a result, the A1 system possesses a longer length of C- *OOH bond than that of A2. These phenomena manifest that the pyranoid-O can tune and redistribute the electronic structure of the adjacent carbon atoms, leading to the passivation of the $^*O-OH$ bond and the activation of the C- *OOH bond to promote the $2e^-$ ORR performance of the carbon material. According to the ORR mechanism of heteroatom-doped carbon materials [58,59], the heteroatom dopants can attract electrons from the adjacent carbon atoms owing to the higher electronegativity, which can conduce to the adsorb of O₂. However, the delocalized nonbonding electrons of heteroatom dopants, such as pyridinic-N will induce the charge from the π orbital to the antibonding orbitals in O₂, which can weaken O-O bond, and subsequently further dissociate into *O and *OH [59]. The π orbital of pyranoid-O has a low delocalization, which can cause the passivation of O-O band, ensuring that the *OOH intermediate subsequently reacts with another proton to form H₂O₂ rather than dissociation route to form H₂O [32].

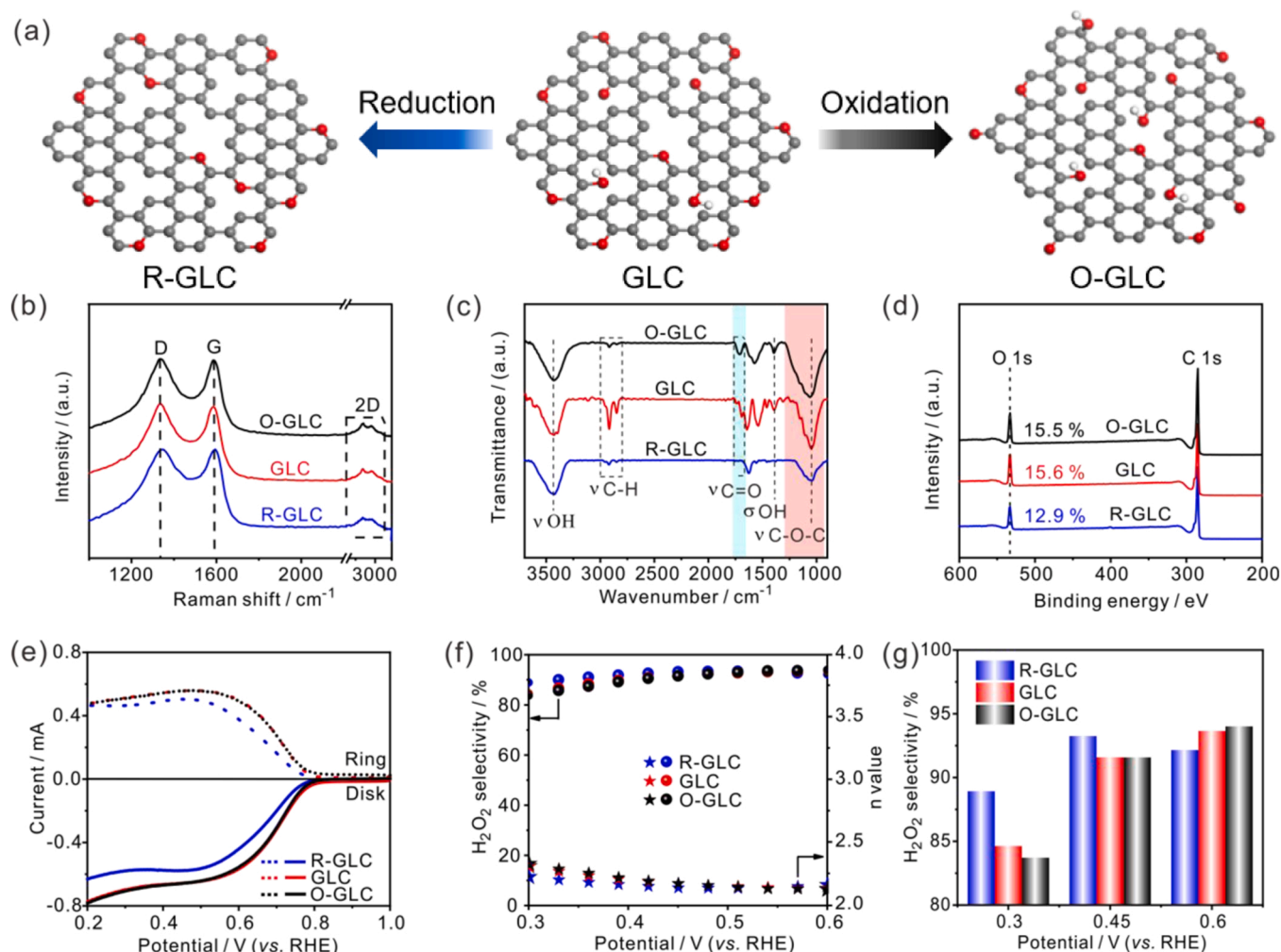


Fig. 7. (a) Schematic diagram, (b) Raman, (c) FTIR, and (d) survey XPS spectra of R-GLC, GLC, and O-GLC (the inset value is content of O 1s in these samples). (e) RRDE polarization curves (solid lines) and detective H₂O₂ currents at ring electrode (dot lines) of R-GLC, GLC, and O-GLC. (f) Calculated n value and H₂O₂ selectivity of R-GLC, GLC, and O-GLC. (g) The H₂O₂ selectivity of R-GLC, GLC, and O-GLC at the potential of 0.3, 0.45, and 0.6 V.

Furthermore, to verify the DFT results, we designed two contrast samples, in which the reduced GLC sample (R-GLC) was obtained by high-temperature H_2 treatment, and the oxidized GLC sample (O-GLC) was fabricated by H_2O_2 oxidation treatment (Fig. 7a). The high-temperature H_2 treatment can remove the surface oxygen-containing groups (e.g., $C=O$, $C-OH$, $COOH$), and ensure that the oxygen dopants such as pyranoid-O, are dominated in carbon material as far as possible [31]. The H_2O_2 oxidation treatment can improve the content of surface oxygen-containing groups [60]. Raman results of Fig. 7b and Table S6 suggest that the I_D/I_G value of O-GLC is almost the same as GLC, whereas R-GLC has a decreased value, indicating that O-GLC possesses a similar defective structure as GLC, but R-GLC has a lower defect degree. As shown in Fig. 7c, the O-GLC sample shows broader and stronger characteristic peaks of oxygen-containing functional groups compared with GLC (especially $C=O$), suggesting the more abundant surface oxygen-containing functional groups in the sample. As for R-GLC, the peak of σOH and $\nu C=O$ were disappeared whereas the $\nu C-O-C$ peaks still exist, suggesting that the residual O atoms are mainly doped into the carbon lattice to form the $C-O-C$ species. The XPS survey spectra of Fig. 7d show that the oxygen percentage of R-GLC (12.91%) is less than that of GLC (15.61%), meaning that the surface oxygen-containing groups may be reduced, and the residual O content may be the oxygen dopants. As shown in Fig. 7e-g, the O-GLC sample displays a similar $2e^-$ ORR performance compared with GLC, indicating that surface oxygen-containing groups are not the key factor for the $2e^-$ ORR. The R-GLC sample shows a deteriorative ORR activity, which may result from the decreased defect degree and graphene edge defects content (Fig. S30). However, the selectivity of R-GLC is even higher than GLC at the low potential range, verifying that the H_2O_2 selectivity is mainly attributed to the pyranoid-O dopants. Notably, the selectivity of the $C=O$ enriched O-GLC sample decreases significantly at lowered potential, whereas the pyranoid-O-dominated R-GLC sample only presents a slight fluctuation. This may be owing to the reduction of ketones to hydroxyls at low potential [5]. In summary, these results indicate that the $2e^-$ ORR selectivity of GLC is mainly attributed to the pyranoid-O dopants, rather than the conventional view of surface oxygen-containing groups [29–32], as also confirmed by our DFT results.

4. Conclusions

In conclusion, we have successfully constructed a graphene-like nanocarbon (GLC) material by using a high-temperature alkali activation method. The obtained GLC not only has graphene-like morphology but also possesses hierarchical porous structure, high surface area, abundant edge defects, as well as plentiful pyranoid-O dopants, conferring it with outperformed $2e^-$ ORR performance. The assembled device based on GLC catalyst achieves a high H_2O_2 yield rate of $1577.33 \text{ mg L}^{-1} \text{ h}^{-1}$ with Faraday efficiency of 95%, along with ultrafast organic waste degradation performance. Most importantly, our described strategy is not limited by the carbonaceous precursor or the alkali active agent, all the obtained carbon products have the similar morphology of GLC and high content of pyranoid-O dopants, which ensure the superior $2e^-$ ORR performance, demonstrating the universal property. DFT calculations reveal that the nature of excellent $2e^-$ selectivity of the materials is highly associated with the pyranoid-O dopants, rather than the surface oxygen-containing functional groups declared by the previous reports, that can redistribute the electronic structure of the carbon matrix to improve the binding affinity for the key intermediate of *OOH , and meanwhile stabilize the $^*O-OH$ bond, for the facilitating of the $2e^-$ ORR process. These results are further supported by a series of controlled experiments. We believe that our developed methods, experimental results, and theoretical observations will be very helpful for the promoting and manufacturing of carbon-based electrocatalysts for environmentally friendly H_2O_2 production and wastewater treatment applications.

CRediT authorship contribution statement

Chang Zhang: Conceptualization, Methodology, Investigation, Formal analysis, Data curation, Writing – original draft. **Wei Liu:** Methodology, Investigation, Formal analysis, Data curation, Writing – original draft. **Min Song:** Investigation, Data curation, Visualization. **Jingjing Zhang:** Investigation, Formal analysis. **Feng He:** Investigation, Visualization. **Jiao Wang:** Investigation, Validation. **Mo Xiong:** Resources, Supervision. **Jian Zhang:** Supervision, Writing – review & editing, Project administration, Funding acquisition. **Deli Wang:** Supervision, Writing – review & editing, Project administration, Funding acquisition.

Declaration of Competing Interest

The authors confirm that this work described has not been published previously, that it is not under consideration for publication elsewhere, that its publication is approved by all authors and explicitly by the responsible authorities where our work was carried out. The authors also agree that, if accepted, it will not be published elsewhere in the same form, in English or in any other language, without the written consent of the Publisher.

Acknowledgments

This work was supported by the National Natural Science Foundation of China (91963109), the Foundation of State Key Laboratory of Coal Combustion (FSKLCCA2008), Open Found of Hubei Key Laboratory of Material Chemistry and Service Failure (2021MCF03), the State Key Laboratory of Advanced Technology for Materials Synthesis and Processing (Wuhan University of Technology) (2021-KF-4), and Key Laboratory of Hubei Province for Coal Conversion and New Carbon Materials (Wuhan University of Science and Technology) (WKDM202101). The authors thank the Analytical and Testing Center of HUST for allowing the support and use of its facilities for Raman and TEM.

Appendix A. Supporting information

Supplementary data associated with this article can be found in the online version at doi:10.1016/j.apcatb.2022.121173.

References

- [1] I. Yamanaka, T. Onizawa, S. Takenaka, K. Otsuka, Direct and Continuous Production of Hydrogen Peroxide with 93% Selectivity Using a Fuel-Cell System, *Angew. Chem.* 115 (2003) 3781–3783, <https://doi.org/10.1002/ange.200351343>.
- [2] C.A. Martinez-Huitle, S. Ferro, Electrochemical oxidation of organic pollutants for the wastewater treatment: direct and indirect processes, *Chem. Soc. Rev.* 35 (2006) 1324–1340, <https://doi.org/10.1039/b517632h>.
- [3] J.M. Campos-Martin, G. Blanco-Brieva, J.L. Fierro, Hydrogen peroxide synthesis: an outlook beyond the anthraquinone process, *Angew. Chem. Int. Ed.* 45 (2006) 6962–6984, <https://doi.org/10.1002/anie.200503779>.
- [4] S. Fukuzumi, Y. Yamada, K.D. Karlin, Hydrogen Peroxide as a Sustainable Energy Carrier: Electrocatalytic Production of Hydrogen Peroxide and the Fuel Cell, *Electrochim. Acta* 82 (2012) 493–511, <https://doi.org/10.1016/j.electacta.2012.03.132>.
- [5] G.F. Han, F. Li, W. Zou, M. Karamad, J.P. Jeon, S.W. Kim, S.J. Kim, Y. Bu, Z. Fu, Y. Lu, S. Siahrostami, J.B. Baek, Building and identifying highly active oxygenated groups in carbon materials for oxygen reduction to H_2O_2 , *Nat. Commun.* 11 (2020) 2209, <https://doi.org/10.1038/s41467-020-15782-z>.
- [6] S. Siahrostami, A. Verdager-Casadevall, M. Karamad, D. Deiana, P. Malacrida, B. Wickman, M. Escudero-Escribano, E.A. Paoli, R. Frydendal, T.W. Hansen, I. Chorkendorff, I.E. Stephens, J. Rossmeisl, Enabling direct H_2O_2 production through rational electrocatalyst design, *Nat. Mater.* 12 (2013) 1137–1143, <https://doi.org/10.1038/nmat3795>.
- [7] Y. Jiang, P. Ni, C. Chen, Y. Lu, P. Yang, B. Kong, A. Fisher, X. Wang, Selective electrochemical H_2O_2 production through two-electron oxygen electrochemistry, *Adv. Energy Mater.* 8 (2018) 1801909, <https://doi.org/10.1002/aenm.201801909>.
- [8] K. Otsuka, I. Yamanaka, One step synthesis of hydrogen peroxide through fuel cell reaction, *Electrochim. Acta* 35 (1990) 319–322, [https://doi.org/10.1016/0013-4686\(90\)87004-L](https://doi.org/10.1016/0013-4686(90)87004-L).

- [9] C. Tang, Y. Zheng, M. Jaroniec, S.-Z. Qiao, Electrocatalytic Refinery for Sustainable Production of Fuels and Chemicals, *Angew. Chem. Int. Ed.* 60 (2021) 19572–19590, <https://doi.org/10.1002/anie.202101522>.
- [10] J. Zhang, L. Zheng, F. Wang, C. Chen, H. Wu, S.A.K. Leghari, M. Long, The critical role of furfural alcohol in photocatalytic H_2O_2 production on TiO_2 , *Appl. Catal. B* 269 (2020), 118770, <https://doi.org/10.1016/j.apcatb.2020.118770>.
- [11] X. Sheng, N. Daems, B. Geboes, M. Kurttepli, S. Bals, T. Breugelmans, A. Hubin, I. F.J. Vankelcom, P.P. Pescarmona, N-doped ordered mesoporous carbons prepared by a two-step nanocasting strategy as highly active and selective electrocatalysts for the reduction of O_2 to H_2O_2 , *Appl. Catal. B* 176–177 (2015) 212–224, <https://doi.org/10.1016/j.apcatb.2015.03.049>.
- [12] Y. Wang, D. Wang, Y. Li, A fundamental comprehension and recent progress in advanced Pt-based ORR nanocatalysts, *SmartMat* 2 (2021) 56–75, <https://doi.org/10.1002/smm2.1023>.
- [13] Y. Sun, L. Silvili, N.R. Sahraie, W. Ju, J. Li, A. Zitolo, S. Li, A. Bagger, L. Arnarson, X. Wang, T. Moeller, D. Bernsmeier, J. Rossmel, F. Jaouen, P. Strasser, Activity-Selectivity Trends in the Electrochemical Production of Hydrogen Peroxide over Single-Site Metal–Nitrogen–Carbon Catalysts, *J. Am. Chem. Soc.* 141 (2019) 12372–12381, <https://doi.org/10.1021/jacs.9b05576>.
- [14] C. Tang, Y. Jiao, B. Shi, J.N. Liu, Z. Xie, X. Chen, Q. Zhang, S.Z. Qiao, Coordination Tunes Selectivity: Two-Electron Oxygen Reduction on High-Loading Molybdenum Single-Atom Catalysts, *Angew. Chem. Int. Ed.* 59 (2020) 9171–9176, <https://doi.org/10.1002/anie.202003842>.
- [15] C. Tang, L. Chen, H. Li, L. Li, Y. Jiao, Y. Zheng, H. Xu, K. Davey, S.-Z. Qiao, Tailoring Acidic Oxygen Reduction Selectivity on Single-Atom Catalysts via Modification of First and Second Coordination Spheres, *J. Am. Chem. Soc.* 143 (2021) 7819–7827, <https://doi.org/10.1021/jacs.1c03135>.
- [16] J. Zhang, J. Zhang, F. He, Y. Chen, J. Zhu, D. Wang, S. Mu, H.Y. Yang, Defect and Doping Co-Engineered Non-Metal Nanocarbon ORR Electrocatalyst, *Nano-Micro Lett.* 13 (2021) 65, <https://doi.org/10.1007/s40820-020-00579-y>.
- [17] S. Chen, Z. Chen, S. Siahrostami, T.R. Kim, D. Nordlund, D. Sokaras, S. Nowak, J. W.F. To, D. Higgins, R. Sinclair, J.K. Nørskov, T.F. Jaramillo, Z. Bao, Defective Carbon-Based Materials for the Electrochemical Synthesis of Hydrogen Peroxide, *ACS Sustain. Chem. Eng.* 6 (2017) 311–317, <https://doi.org/10.1021/acssuschemeng.7b02517>.
- [18] Y. Hu, J. Zhang, T. Shen, Z. Li, K. Chen, Y. Lu, J. Zhang, D. Wang, Efficient Electrochemical Production of H_2O_2 on Hollow N-Doped Carbon Nanospheres with Abundant Micropores, *ACS Appl. Mater. Interfaces* 13 (2021) 29551–29557, <https://doi.org/10.1021/acsami.1c05353>.
- [19] L. Wang, K. Liang, L. Deng, Y.-N. Liu, Protein hydrogel networks: A unique approach to heteroatom self-doped hierarchically porous carbon structures as an efficient ORR electrocatalyst in both basic and acidic conditions, *Appl. Catal. B* 246 (2019) 89–99, <https://doi.org/10.1016/j.apcatb.2019.01.050>.
- [20] J. Zhu, Y. Huang, W. Mei, C. Zhao, C. Zhang, J. Zhang, I.S. Amiin, S. Mu, Effects of Intrinsic Pentagon Defects on Electrochemical Reactivity of Carbon Nanomaterials, *Angew. Chem. Int. Ed.* 58 (2019) 3859–3864, <https://doi.org/10.1002/anie.201813805>.
- [21] C.Y. Chen, C. Tang, H.F. Wang, C.M. Chen, X. Zhang, X. Huang, Q. Zhang, Oxygen Reduction Reaction on Graphene in an Electro-Fenton System: In Situ Generation of H_2O_2 for the Oxidation of Organic Compounds, *ChemSusChem* 9 (2016) 1194–1199, <https://doi.org/10.1002/cssc.201600030>.
- [22] M. Zhang, H. Tao, Y. Liu, C. Yan, S. Hong, J. Masa, A.W. Robertson, S. Liu, J. Qiu, Z. Sun, Ultrasound-assisted nitrogen and boron codoping of graphene oxide for efficient oxygen reduction reaction, *ACS Sustain. Chem. Eng.* 7 (2019) 3434–3442, <https://doi.org/10.1021/acssuschemeng.8b05654>.
- [23] H.-S. Zhai, L. Cao, X.-H. Xia, Synthesis of graphitic carbon nitride through pyrolysis of melamine and its electrocatalysis for oxygen reduction reaction, *Chin. Chem. Lett.* 24 (2013) 103–106, <https://doi.org/10.1016/j.ccl.2013.01.030>.
- [24] M. Sun, C. Zhang, D. Chen, J. Wang, Y. Ji, N. Liang, H. Gao, S. Cheng, H. Liu, Ultrasensitive and stable all graphene field-effect transistor-based Hg^{2+} sensor constructed by using different covalently bonded RGO films assembled by different conjugate linking molecules, *SmartMat* 2 (2021) 213–225, <https://doi.org/10.1002/smm2.1030>.
- [25] B. Xu, S. Qi, M. Jin, X. Cai, L. Lai, Z. Sun, X. Han, Z. Lin, H. Shao, P. Peng, Z. Xiang, J.E. ten Elshof, R. Tan, C. Liu, Z. Zhang, X. Duan, J. Ma, 2020 roadmap on two-dimensional materials for energy storage and conversion, *Chin. Chem. Lett.* 30 (2019) 2053–2064, <https://doi.org/10.1016/j.ccl.2019.10.028>.
- [26] S. Wu, Q. He, C. Tan, Y. Wang, H. Zhang, Graphene-based electrochemical sensors, *Small* 9 (2013) 1160–1172, <https://doi.org/10.1002/sml.201202896>.
- [27] D. Bitounis, H. Ali-Boucetta, B.H. Hong, D.H. Min, K. Kostarelos, Prospects and challenges of graphene in biomedical applications, *Adv. Mater.* 25 (2013) 2258–2268, <https://doi.org/10.1002/adma.201203700>.
- [28] J. Chen, C. Li, G. Shi, Graphene Materials for Electrochemical Capacitors, *J. Phys. Chem. Lett.* 4 (2013) 1244–1253, <https://doi.org/10.1021/jz400160k>.
- [29] Z. Lu, G. Chen, S. Siahrostami, Z. Chen, K. Liu, J. Xie, L. Liao, T. Wu, D. Lin, Y. Liu, T.F. Jaramillo, J.K. Nørskov, Y. Cui, High-efficiency oxygen reduction to hydrogen peroxide catalysed by oxidized carbon materials, *Nat. Catal.* 1 (2018) 156–162, <https://doi.org/10.1038/s41929-017-0017-x>.
- [30] S. Chen, T. Luo, K. Chen, Y. Lin, J. Fu, K. Liu, C. Cai, Q. Wang, H. Li, X. Li, J. Hu, H. Li, M. Zhu, M. Liu, Chemical Identification of Catalytically Active Sites on Oxygen-doped Carbon Nanosheet to Decipher the High Activity for Electro-synthesis Hydrogen Peroxide, *Angew. Chem. Int. Ed.* 60 (2021) 2–10, <https://doi.org/10.1002/anie.202104480>.
- [31] F. Sun, C. Yang, Z. Qu, W. Zhou, Y. Ding, J. Gao, G. Zhao, D. Xing, Y. Lu, Inexpensive activated coke electrocatalyst for high-efficiency hydrogen peroxide production: Coupling effects of amorphous carbon cluster and oxygen dopant, *Appl. Catal. B* 286 (2021), 119860, <https://doi.org/10.1016/j.apcatb.2020.119860>.
- [32] C. Zhang, J. Zhang, J. Zhang, M. Song, X. Huang, W. Liu, M. Xiong, Y. Chen, S. Xia, H. Yang, D. Wang, Tuning Coal into Graphene-Like Nanocarbon for Electrochemical H_2O_2 Production with Nearly 100% Faraday Efficiency, *ACS Sustain. Chem. Eng.* 9 (2021) 9369–9375, <https://doi.org/10.1021/acssuschemeng.1c02357>.
- [33] J. Zhang, H. Zhou, J. Zhu, P. Hu, C. Hang, J. Yang, T. Peng, S. Mu, Y. Huang, Facile Synthesis of Defect-Rich and S/N Co-Doped Graphene-Like Carbon Nanosheets as an Efficient Electrocatalyst for Primary and All-Solid-State Zn-Air Batteries, *ACS Appl. Mater. Interfaces* 9 (2017) 24545–24554, <https://doi.org/10.1021/acsami.7b04665>.
- [34] M.G. Stanford, K.V. Bets, D.X. Luong, P.A. Advincula, W. Chen, J.T. Li, Z. Wang, E. A. McHugh, W.A. Algozeeb, B.I. Yakobson, J.M. Tour, Flash Graphene Morphologies, *ACS Nano* 14 (2020) 13691–13699, <https://doi.org/10.1021/acsnano.0c05900>.
- [35] U. Lee, Y.S. Woo, Y. Han, H.R. Gutierrez, U.J. Kim, H. Son, Facile Morphological Qualification of Transferred Graphene by Phase-Shifting Interferometry, *Adv. Mater.* 32 (2020) 2002854, <https://doi.org/10.1002/adma.202002854>.
- [36] J. Xu, X. Cui, N. Liu, Y. Chen, H.W. Wang, Structural engineering of graphene for high-resolution cryo-electron microscopy, *SmartMat* 2 (2021) 202–212, <https://doi.org/10.1002/smm2.1045>.
- [37] X. Wen, D. Zhang, T. Yan, J. Zhang, L. Shi, Three-dimensional graphene-based hierarchically porous carbon composites prepared by a dual-template strategy for capacitive deionization, *J. Mater. Chem. A* 1 (2013), <https://doi.org/10.1039/c3ta12683h>.
- [38] J. Zhang, Y. Sun, J. Zhu, Z. Kou, P. Hu, L. Liu, S. Li, S. Mu, Y. Huang, Defect and pyridinic nitrogen engineering of carbon-based metal-free nanomaterial toward oxygen reduction, *Nano Energy* 52 (2018) 307–314, <https://doi.org/10.1016/j.nanoen.2018.08.003>.
- [39] J. Park, Y. Nabee, T. Hayakawa, M.-a. Kakimoto, Highly Selective Two-Electron Oxygen Reduction Catalyzed by Mesoporous Nitrogen-Doped Carbon, *ACS Catal.* 4 (2014) 3749–3754, <https://doi.org/10.1021/cs5008206>.
- [40] T. Jawhari, A. Roid, J. Casado, Raman spectroscopic characterization of some commercially available, Carbon Black Mater., *Carbon* 33 (1995) 1561–1565, [https://doi.org/10.1016/0008-6223\(95\)00117-V](https://doi.org/10.1016/0008-6223(95)00117-V).
- [41] A. Sadezy, H. Muckenhuber, H. Grothe, R. Niessner, U. Pöschl, Raman microspectroscopy of soot and related carbonaceous materials: Spectral analysis and structural information, *Carbon* 43 (2005) 1731–1742, <https://doi.org/10.1016/j.carbon.2005.02.018>.
- [42] B.Q. Li, C.X. Zhao, J.N. Liu, Q. Zhang, Electrosynthesis of Hydrogen Peroxide Synergistically Catalyzed by Atomic Co-Nx-C Sites and Oxygen Functional Groups in Noble-Metal-Free Electrocatalysts, *Adv. Mater.* 31 (2019), e1808173, <https://doi.org/10.1002/adma.201808173>.
- [43] H.W. Kim, M.B. Ross, N. Kornienko, L. Zhang, J. Guo, P. Yang, B.D. McCloskey, Efficient hydrogen peroxide generation using reduced graphene oxide-based oxygen reduction electrocatalysts, *Nat. Catal.* 1 (2018) 282–290, <https://doi.org/10.1038/s41929-018-0044-2>.
- [44] Y.J. Sa, J.H. Kim, S.H. Joo, Active Edge-Site-Rich Carbon Nanocatalysts with Enhanced Electron Transfer for Efficient Electrochemical Hydrogen Peroxide Production, *Angew. Chem. Int. Ed.* 58 (2019) 1100–1105, <https://doi.org/10.1002/anie.201812435>.
- [45] C. Zhang, G. Liu, B. Ning, S. Qian, D. Zheng, L. Wang, Highly efficient electrochemical generation of H_2O_2 on N/O co-modified defective carbon, *Int. J. Hydro. Energy* 46 (2021) 14277–14287, <https://doi.org/10.1016/j.ijhydene.2021.01.195>.
- [46] D. Wang, S. Li, X. Zhang, B. Feng, Y. Pei, Y. Zhu, W. Xu, Z.-H. Li, M. Qiao, B. Zong, Pyrolyzed polydopamine-modified carbon black for selective and durable electrocatalytic oxygen reduction to hydrogen peroxide in acidic medium, *Appl. Catal. B* 305 (2022), 121036, <https://doi.org/10.1016/j.apcatb.2021.121036>.
- [47] L. Hao, S. Zhang, R. Liu, J. Ning, G. Zhang, L. Zhi, Bottom-up construction of triazine-based frameworks as metal-free electrocatalysts for oxygen reduction reaction, *Adv. Mater.* 27 (2015) 3190–3195, <https://doi.org/10.1002/adma.201500863>.
- [48] Q. Yang, Z. Xiao, D. Kong, T. Zhang, X. Duan, S. Zhou, Y. Niu, Y. Shen, H. Sun, S. Wang, L. Zhi, New insight to the role of edges and heteroatoms in nanocarbons for oxygen reduction reaction, *Nano Energy* 66 (2019), 104096, <https://doi.org/10.1016/j.nanoen.2019.104096>.
- [49] S. Yang, Q. Cheng, J. Mao, Q. Xu, Y. Zhang, Y. Guo, T. Tan, W. Luo, H. Yang, Z. Jiang, Rational Design of Edges of Covalent Organic Networks for Catalyzing Hydrogen Peroxide Production, *Appl. Catal. B* (2021), 120605, <https://doi.org/10.1016/j.apcatb.2021.120605>.
- [50] J. Zhu, X. Xiao, K. Zheng, F. Li, G. Ma, H.-C. Yao, X. Wang, Y. Chen, KOH-treated reduced graphene oxide: 100% selectivity for H_2O_2 electroproduction, *Carbon* 153 (2019) 6–11, <https://doi.org/10.1016/j.carbon.2019.07.009>.
- [51] L. Zhou, J. Lei, F. Wang, L. Wang, M.R. Hoffmann, Y. Liu, S.-I. In, J. Zhang, Carbon nitride nanotubes with in situ grafted hydroxyl groups for highly efficient spontaneous H_2O_2 production, *Appl. Catal. B* 288 (2021), 119993, <https://doi.org/10.1016/j.apcatb.2021.119993>.
- [52] Y. Hu, Y. Li, J. He, T. Liu, K. Zhang, X. Huang, L. Kong, J. Liu, EDTA-Fe(III) Fenton-like oxidation for the degradation of malachite green, *J. Environ. Manag.* 226 (2018) 256–263, <https://doi.org/10.1016/j.jenvman.2018.08.029>.
- [53] S.J. Culp, L.R. Blankenship, D.F. Kusewitt, D.R. Doerge, L.T. Mulligan, F.A. Beland, Toxicity and metabolism of malachite green and leucomalachite green during short-term feeding to Fischer 344 rats and B6C3F1 mice, *Chem. Biol. Interact.* 122 (1999) 153–170, [https://doi.org/10.1016/S0009-2797\(99\)00119-2](https://doi.org/10.1016/S0009-2797(99)00119-2).

- [54] J. Li, Y. Li, Z. Xiong, G. Yao, B. Lai, The electrochemical advanced oxidation processes coupling of oxidants for organic pollutants degradation: A mini-review, *Chin. Chem. Lett.* 30 (2019) 2139–2146, <https://doi.org/10.1016/j.ccllet.2019.04.057>.
- [55] R. Guo, Y. Wang, J. Li, X. Cheng, D.D. Dionysiou, Sulfamethoxazole degradation by visible light assisted peroxymonosulfate process based on nanohybrid manganese dioxide incorporating ferric oxide, *Appl. Catal. B* 278 (2020), 119297, <https://doi.org/10.1016/j.apcatb.2020.119297>.
- [56] L. Zhang, Z. Xia, Mechanisms of Oxygen Reduction Reaction on Nitrogen-Doped Graphene for Fuel Cells, *J. Phys. Chem. C* 115 (2011) 11170–11176, <https://doi.org/10.1021/jp201991j>.
- [57] X. Zhao, Y. Liu, Origin of Selective Production of Hydrogen Peroxide by Electrochemical Oxygen Reduction, *J. Am. Chem. Soc.* 143 (2021) 9423–9428, <https://doi.org/10.1021/jacs.1c02186>.
- [58] L. Li, C. Tang, Y. Zheng, B. Xia, X. Zhou, H. Xu, S.-Z. Qiao, Tailoring Selectivity of Electrochemical Hydrogen Peroxide Generation by Tunable Pyrrolic-Nitrogen-Carbon, *Adv. Energy Mater.* 10 (2020) 2000789, <https://doi.org/10.1002/aenm.202000789>.
- [59] D. Guo, R. Shibuya, C. Akiba, S. Saji, T. Kondo, J. Nakamura, Active sites of nitrogen-doped carbon materials for oxygen reduction reaction clarified using model catalysts, *Science* 351 (2016) 361–365, <https://doi.org/10.1126/science.aad0832>.
- [60] S.H. Ahn, K.J. Cluff, N. Bhuvanesh, J. Blumel, Hydrogen Peroxide and Di (hydroperoxy)propane Adducts of Phosphine Oxides as Stoichiometric and Soluble Oxidizing Agents, *Angew. Chem. Int. Ed.* 54 (2015) 13341–13345, <https://doi.org/10.1002/anie.201505291>.